Membrane curvature underlies actin reorganization in response to nanoscale surface topography

Hsin-Ya Lou[a,1], Wenting Zhao[a,b,1], Xiao Li[a], Liting Duan[a], Alexander Powers[a], Matthew Akamatsu[c], Francesca Santoro[a], Allister F. McGuire[a], Yi Cui[b], David G. Drubin[c], and Bianxiao Cui[a,2]

[a]Department of Chemistry, Stanford University, Stanford, CA 94305; [b]Department of Materials Science and Engineering, Stanford University, Stanford, CA 94305; and [c]Department of Molecular & Cell Biology, University of California, Berkeley, CA 94720

Edited by Charles M. Lieber, Harvard University, Cambridge, MA, and approved September 17, 2019 (received for review June 14, 2019)

Surface topography profoundly influences cell adhesion, differentiation, and stem cell fate control. Numerous studies using a variety of materials demonstrate that nanoscale topographies change the intracellular organization of actin cytoskeleton and therefore a broad range of cellular dynamics in live cells. However, the underlying molecular mechanism is not well understood, leaving why actin cytoskeleton responds to topographical features unexplained and therefore preventing researchers from predicting optimal topographic features for desired cell behavior. Here we demonstrate that topography-induced membrane curvature plays a crucial role in modulating intracellular actin organization. By inducing precisely controlled membrane curvatures using engineered vertical nanostructures as topographies, we find that actin fibers form at the sites of nanostructures in a curvature-dependent manner with an upper limit for the diameter of curvature at ∼400 nm. Nanotopography-induced actin fibers are branched actin nucleated by the Arp2/3 complex and are mediated by a curvature-sensing protein FBP17. Our study reveals that the formation of nanotopography-induced actin fibers drastically reduces the amount of stress fibers and mature focal adhesions to result in the reorganization of actin cytoskeleton in the entire cell. These findings establish the membrane curvature as a key linkage between surface topography and topography-induced cell signaling and behavior.

surface topography | membrane curvature | nano–bio interface | actin polymerization | F-BAR proteins

Extensive experimental studies have shown that surface topography on the scale of tens of nanometers to a few micrometers markedly influences stem cell differentiation, cell adhesion, migration, and host–implant integration (1–4). For example, nanotopography has been demonstrated to enhance the differentiation of human mesenchymal stem cells (5, 6), steering neural stem cells toward neuronal lineage (7, 8), and modulating macrophage activities (9). Actin cytoskeleton, an essential component involved in many cellular behaviors, has been reported to be significantly affected by surface topography. Dense and nanoscale pillar structured topographies were shown to reduce the total amount of long actin stress fibers in cells (10–12). Sparse nanostructures were shown to induce local accumulation of actin fibers in a variety of cell types (13–16).

Despite numerous efforts, the underlying molecular mechanisms of why nanotopography induces actin reorganization remain unclear. Several hypotheses have been proposed, which include the nanofabrication process changing the surface chemistry (17), nanotopography increasing the surface area (18–20), or the 2D organization of topographic features leads to discontinuities and clustering of adhesion ligands (21, 22). However, more studies over the years contest these hypotheses by showing that the size and the local shape of topographic features significantly affect cellular responses (3, 23, 24). Up to date, the precise sets of topographic cues that elicit actin reorganization are yet to be determined.

Electron microscopy and fluorescence studies show that nanostructures protruding from the substrate surface induce membrane wrapping in 3D and thus generate local curvatures on the plasma membrane (25–27). Our recent study shows that these nanotopography-induced membrane curvatures can be recognized by intracellular curvature-sensing proteins to significantly enhance clathrin-dependent endocytosis (28). In the same study, we found that filamentous actin (F-actin) accumulated strongly at the nanotopography locations, a phenomenon also observed in previous studies (15). However, it is unclear whether F-actin accumulation is induced by local membrane curvatures either through clathrin-dependent endocytosis or through other molecular mechanisms.

In this work, we aim to elucidate the molecular mechanisms of topography-induced actin reorganization in cells. Using precisely engineered topographic nanostructures, we demonstrate that nanoscale topographies induce local accumulations of actin filaments in a curvature-dependent manner. We further show that topography-induced membrane curvatures are recognized by intracellular curvature-sensing protein FBP17, which induces the formation of branched F-actin through N-WASP, Cortactin, and Arp2/3. The curvature-mediated actin polymerization results in whole-cell reorganization of actin fibers and significantly reduces the amount of stress fibers and mature focal adhesions.

Results and Discussion

Nanotopography Induced F-Actin Accumulation Is Curvature Dependent. Arrays of SiO_2 nanopillars with well-defined geometry (diameter of 100 to 1,000 nm, height of 1 to 2 μm, and interpillar distance of 2 to 5 μm) are fabricated using top-down e-beam lithography

Significance

Despite a large body of work, little is known about the origin or underlying mechanisms of how cells interact with surface topographic patterns, which has resulted in a primarily phenomenological approach in studying cell–nanotopography interactions. This study illustrates that membrane curvatures induced by nanoscale surface topography can serve as a direct biochemical signal to activate curvature-sensing protein and regulate actin polymerization and mechanotransduction in the intracellular space.

Author contributions: H.-Y.L., W.Z., Y.C., D.G.D., and B.C. designed research; H.-Y.L., W.Z., X.L., L.D., M.A., F.S., and A.F.M. performed research; H.-Y.L., W.Z., X.L., A.P., and B.C. contributed new reagents/analytic tools; H.-Y.L., W.Z., X.L., and A.P. analyzed data; and H.-Y.L., W.Z., D.G.D., and B.C. wrote the paper.

The authors declare no competing interest.

This article is a PNAS Direct Submission.

See Commentary on page 22897.

[1]H.-Y.L. and W.Z. contributed equally to this work.

[2]To whom correspondence may be addressed. Email: bcui@stanford.edu.

This article contains supporting information online at www.pnas.org/lookup/suppl/doi:10.1073/pnas.1910166116/-/DCSupplemental.

First published October 7, 2019.

(EBL) and reactive ion etching on SiO_2 substrates (Fig. 1*A*). Here, the surface chemistry is identical across both the nanostructures and flat areas as they are made of the same material and processed through the same chemical procedure. When U2OS cells are cultured on nanopillar substrates, their plasma membranes wrap around nanopillars as shown by both scanning electron microscopy (SEM) (Fig. 1*B*) and focused ion beam (FIB)/SEM in our previous study (25). Therefore, vertical nanopillars induce local membrane curvatures with a curvature value determined by the nanopillar diameter (29). The largest contribution to membrane curvature is from tight wrapping around the sidewall, which has a 10 times larger area than the top. Confocal fluorescence imaging of U2OS cells transfected with Lifeact-RFP (an F-actin marker) shows that F-actin distributes along the sidewall and the top of nanopillars (*SI Appendix*, Fig. S1*A*). F-actin visualized by phalloidin staining shows significant accumulation at nanopillars of 3 different diameters (arrowheads in Fig. 1*C*) compared to the surrounding flat area.

To study the effect of different membrane curvatures on F-actin accumulation within the same cell, we engineered a gradient array with nanopillar diameters ranging from 100 nm to 1,000 nm (Fig. 1*D* and *SI Appendix*, Fig. S1*C*). For a single U2OS cell covering a range of nanopillar diameters, F-actin accumulation is often stronger on small nanopillars than on larger ones in the same cell (Fig. 1*E*). We note that a vertical nanopillar presents an increased membrane area in a projected 2D fluorescence image, and thus the enhanced F-actin signal at nanopillar locations could be due to the increased actin cortex associated with the projected plasma membrane area. To quantify the differences on nanopillars of different diameters, we separately averaged the fluorescence signals of F-actin and GFP-CAAX, a plasma membrane marker, over hundreds of nanopillars for each diameter (Fig. 1*F* and *SI Appendix*, Fig. S1 *D–F*). Both F-actin and GFP-CAAX appear as rings on large-diameter nanopillars and dots on small-diameter ones due to the diffraction limit of the light. Above 400 nm, the normalized F-actin signal by the GFP-CAAX signal stays relatively constant as the nanopillar diameter increases further (Fig. 1*G*), suggesting that the F-actin rings around large nanopillars are likely due to the increased membrane area at nanopillar locations. In contrast, as the nanopillar diameter decreases from 400 nm to 100 nm, the normalized F-actin signal increases significantly. This trend is preserved when using the supported lipid bilayer as the reference for surface area (*SI Appendix*, Fig. S1 *G* and *H*). The increased F-actin accumulation

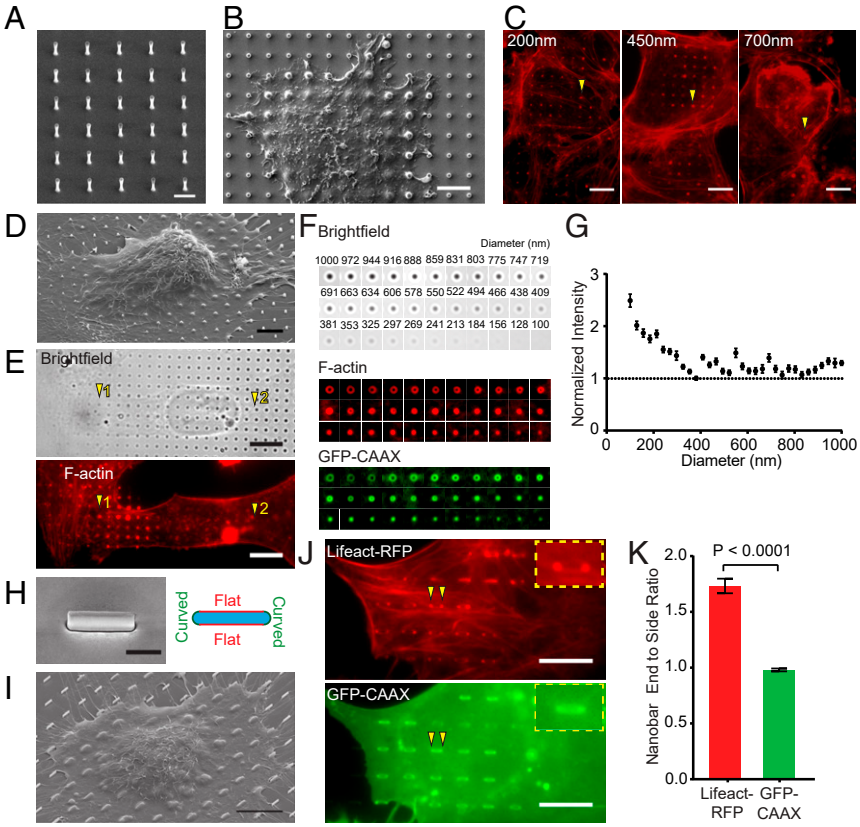

Fig. 1. Vertical nanostructure-induced actin polymerization is curvature dependent. (*A*) An SEM image of a vertical SiO_2 nanopillar array with 2-μm height, 3-μm center-to-center distance, and 400-nm diameter. (*B*) An SEM image shows the deformation of the plasma membrane by nanopillars. (*C*) Phalloidin staining shows F-actin accumulation around vertical nanopillars with 200-, 450-, and 700-nm diameters. The height and center-to-center distance of the nanopillars are 2 μm and 4 μm, respectively. (*D*) An SEM image of a U2OS cell cultured on a gradient nanopillar array covering a range of nanopillar diameters. (*E*) On a gradient nanopillar array, phalloidin staining shows stronger F-actin accumulation on small-diameter nanopillars than large ones (1 versus 2) in the same cell. (*F*) The average images of brightfield, F-actin, and GFP-CAAX on nanopillars with 33 different diameters, from the largest to the smallest. $n = 235$ to 452 (see *SI Appendix*, Table S1 for detailed statistics). (*G*) F-actin signal normalized by the GFP-CAAX signal increased when the nanopillar diameter decreases below 400 nm. (*H*, *Left*) An SEM image of a nanobar with 200-nm width, 2-μm length, and 1-μm height. (*H*, *Right*) A schematic illustrates 2 different vertical membrane curvatures: high curvatures at the ends and flat curvature along the sidewalls of a nanobar. (*I*) An SEM image of a U2OS cell cultured on nanobar arrays outlines the top cell membrane deformed by nanobars. (*J*) A U2OS cell cotransfected with Life-RFP and GFP-CAAX shows that Lifeact-RFP accumulates on the nanobar ends while GFP-CAAX distributes relatively evenly along the length of the same nanobar (arrowheads). (*K*) Quantified nanobar end-to-side ratios for Lifeact-RFP and GFP-CAAX, $n = 438$ nanopillars for both proteins. Welch's *t* test (2 tailed, unpaired, assuming unequal SD). Error bars represent SEM. (*G* and *K*). (Scale bars, 2 μm [*A*], 5 μm [*B* and *D*], 10 μm [*C*, *E*, *I*, and *J*], and 1 μm [*H*].)

at small-diameter nanopillars indicates that actin polymerization is correlated with high membrane curvature. Detailed statistics are listed in *SI Appendix*, Table S1. We note that the SD is always large despite measuring many nanopillars and cells. This is because F-actin accumulations are highly dynamic (discussed later) and only appear on a subset of nanopillars at any given time. We use SD of the mean to indicate the confidence of averaged values.

To further verify the curvature dependence of F-actin accumulation, we engineered nanobars (2,000-nm length, 200-nm width, 1,000-nm height, and 5,000-nm spacing) that induce 2 different vertical membrane curvatures—high curvature at the bar ends and low curvature along the sidewalls (Fig. 1*H*). When cultured on nanobar arrays, U2OS cells wrap around the sidewalls of nanobars (Fig. 1*I*), which is shown in a FIB/SEM investigation of the interface (*SI Appendix*, Fig. S1*B*). To visualize F-actin and the plasma membrane simultaneously, U2OS cells were cotransfected with a F-actin marker Lifeact-RFP and a membrane marker GFP-CAAX. Lifeact-RFP accumulates strongly at nanobar ends, whereas GFP-CAAX distributed relatively evenly along the entire length of the same nanobar in the same cell (arrowheads in Fig. 1*J*). Similar to what is observed on nanopillars, there is usually a large variation in F-actin responses to individual nanobars even in the same cell. By calculating the averaged intensity ratio between the nanobar end and sidewalls from 438 nanobars, we show that Lifeact-RFP gives a strong preference to the nanobar end, while GFP-CAAX shows little preference (Fig. 1*K*). It confirms that F-actin accumulation on nanostructures is strongly correlated with the value of the membrane curvature. In the following studies, we used nanopillars of 200-nm diameter and nanobars of 200-nm width, both of which induce strong curvature-dependent F-actin polymerization.

Membrane Curvature Induces the Formation of Branched F-Actin Nucleated by the Arp2/3 Complex. Actin polymerization is mainly initiated by 2 types of actin nucleators: the Arp2/3 complex and formins (Fig. 2*A*). The Arp2/3 complex induces the formation of branched F-actin while formins promote the growth of linear F-actin (30). When U2OS cells were transfected with Arp3-GFP, a subunit of the Arp2/3 complex, we observed distinct local accumulation of Arp3-GFP at the ends of nanobars with very little signal along the sidewalls (Fig. 2*B*). A similar distribution of endogenous Arp2/3 complex with a strong bias toward the ends of nanobars is also observed by anti-Arp2/3 immunostaining in untransfected cells (*SI Appendix*, Fig. S2*A*). In sharp contrast to Arp3, mDia1-Emerald and mDia2-Emerald, 2 members of the formin family proteins, show no preferential accumulation at the ends of nanobars (Fig. 2*C* and the corresponding full images in *SI Appendix*, Fig. S2*B*).

Moreover, Arp2/3 nucleation promoting factors, N-WASP and Cortactin (31) also exhibit curvature-dependent accumulation at the end of the nanobars (Fig. 2*D* and the corresponding full images in *SI Appendix*, Fig. S2*C*), which show much higher end-to-side ratio than the membrane control (mCherry-CAAX) does (Fig. 2*E*). We note that the visibly higher end-to-side ratio of Arp3-GFP, N-WASP-GFP, and GFP-Cortactin in comparison to mCherry-CAAX were always confirmed in the same batch of cotransfection experiments, but the quantified values for the same protein vary from experiment to experiment due to large variations in protein expression levels. Cotransfection of Arp3-GFP, N-WASP-GFP, or GFP-Cortactin with Lifeact-RFP shows that all 3 proteins strongly colocalize with F-actin on nanopillars (Fig. 2 *F*–*H*). The spatial preference of Arp2/3, N-WASP, and Cortactin on the ends of nanobars and their colocalization with F-actin suggests that Arp2/3-nucleated branched actin, rather

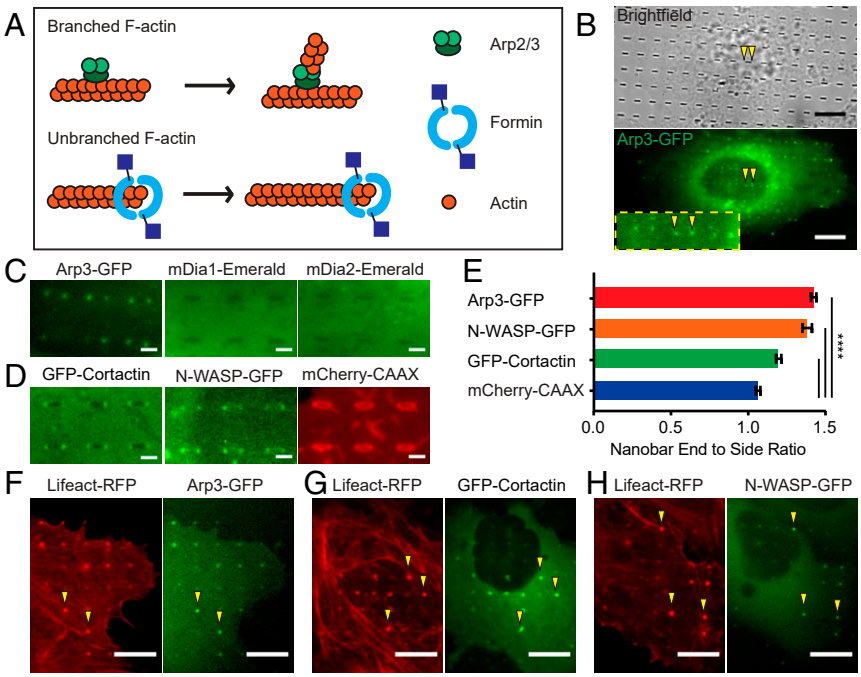

Fig. 2. Nanostructure-induced F-actin is branched F-actin nucleated by Arp2/3. (*A*) A schematic illustration of actin nucleators, Arp2/3 and formin, involved in polymerizing branched and linear actin filaments, respectively. (*B*) Live-cell imaging shows that Arp3-GFP strongly accumulates at the ends of nanobars (arrowheads). (*C*) Zoomed-in fluorescence images of Arp3-GFP, mDia1-Emerald, or mDia2-Emerald in U2OS cells show that only Arp3-GFP accumulates at the ends of nanobars (see *SI Appendix*, Fig. S2*B* for the full images). (*D*) Zoomed-in fluorescence images of GFP-Cortactin, N-WASP-GFP, and mCherry-CAAX show strong accumulation of GFP-Cortactin and N-WASP-GFP to the ends of nanobars (see *SI Appendix*, Fig. S2*C* for the full images). (*E*) Quantification of the nanobar-end-to-side ratio for Arp3-GFP, N-WASP-GFP, GFP-Cortactin, and mCherry-CAAX, $n = 789$ to 2,746 nanobars (see *SI Appendix*, Table S2 for detailed statistics). (*F*–*H*) Live-cell fluorescence images of cotransfected cells show that F-actin marker Lifeact colocalizes with Arp3 (*F*), Cortactin (*G*), and N-WASP (*H*). Welch's *t* test, *P* value indicated in *E*, ****$P < 0.0001$; error bars represent SEM. (Scale bars, 10 μm [*B*] and 2 μm [*C* and *D*].)

than formin-nucleated linear actin, accumulates on nanostructures in a curvature-dependent manner.

Nanostructure-Induced F-Actin Accumulation on Nanostructures Is Highly Dynamic. In cells, F-actin usually undergoes rapid assembly or disassembly in order to afford cell adhesion, migration, morphogenesis, or force generation. Here, we show that nanostructure-induced F-actin accumulation also exhibits fast dynamics. As shown in Fig. 3*A*, the kymograph of Lifeact-RFP exhibits characteristic "blinking events" on nanopillars, indicating that F-actin on nanopillars is not stationary but constantly depolymerizes and repolymerizes in a time-dependent manner. The dynamic on–off behavior of F-actin accumulation is apparent on small nanopillars (Movie S1). On the other hand, the F-actin rings around large nanopillars are relatively stable, agreeing with the notion that the F-actin rings around large nanopillars are of a different process and likely due to the increased membrane area around large nanopillars. Quantitative analysis of Lifeact-RFP dynamics indicates that F-actin assembles and disassembles with a frequency of ~0.4/min (Fig. 3*C*). Single cell measurements show that drug inhibition of Arp2/3 using inhibitor CK666 significantly reduces the dynamic fluctuations of F-actin on nanopillars (Fig. 3*C*). In contrast, a formin FH2 inhibitor SMIFH2 did not perturb F-actin dynamics on nanopillars (Fig. 3*D*).

Furthermore, Arp2/3, N-WASP, and Cortactin also exhibit highly synchronized dynamic with F-actin on nanopillars (Fig. 3 *E* and *F* and Movies S2–S4). On the other hand, neither mDia1-Emerald nor mDia2-Emerald shows observable accumulations or dynamic fluctuations on nanopillars. The dynamic correlation between F-actin and actin-related proteins on nanopillars was further evaluated by using Pearson correlation coefficients (Fig. 3*G*). The correlation coefficients between Lifeact-RFP and Arp3-GFP (0.68 ± 0.02, SEM), GFP-Cortactin (0.69 ± 0.02), and N-WASP-GFP (0.54 ± 0.02) indicate high-level correlation. On the other hand, mDia1-Emerald (0.04 ± 0.02) and mDia2-Emerald (0.09 ± 0.01) show very little correlation. The temporal correlation of F-actin with Arp3, N-WASP, and Cortactin further confirms the involvement of these proteins in nanotopography-induced F-actin assembly.

Curvature Sensing Protein, FBP17, Mediates the Branched F-Actin Formation at Nanotopography-Induced Membrane Curvatures. Neither Arp2/3 complex nor its nucleation promoting factors are known to recognize membrane curvatures. Their connecting factor is the key to understand the underlying molecular mechanism of the topography-triggered F-actin formation. Here, we hypothesize that curvature-sensitive BAR proteins (32) can serve the role of bridging actin polymerization with membrane curvature. In mammalian cells, the Toca F-BAR family, including FBP17, Toca-1, and CIP4, are known to contain an N-terminal F-BAR domain that senses membrane curvature, and a C-terminal SH3 domain that interacts with N-WASP and cdc42

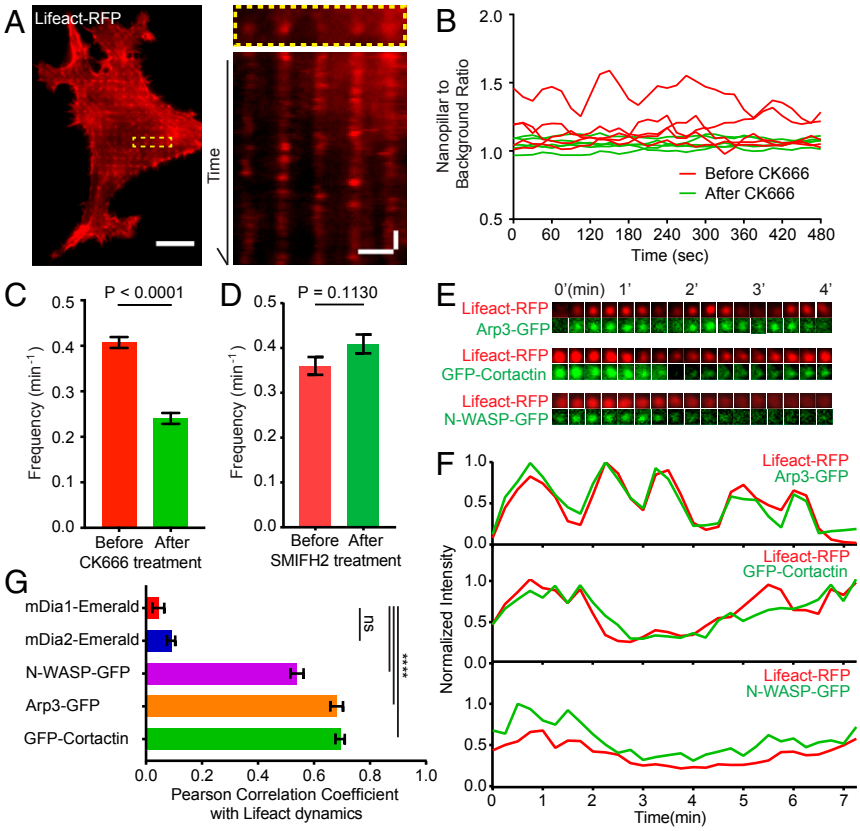

Fig. 3. Curvature-dependent F-actin accumulation on nanostructures is highly dynamic. (*A*, *Left*) A time-lapse image of a cell transfected with Lifeact-RFP (Movie S1). (*A*, *Right*) A kymograph plot shows that Lifeact-RFP signals on nanopillars repeatedly appear and disappear. (*B*) Representative trajectories of F-actin dynamics before and after CK666 treatment. (*C*) Kinetic analysis shows that F-actin dynamics on nanopillars are significantly reduced by Arp2/3 inhibitor CK666. (*D*) A formin inhibitor SMIFH2 does not alter F-actin dynamics on nanopillars. (*E* and *F*) Time-lapse images of Lifeact-RFP with Arp3-GFP, Lifeact-RFP with GFP-Cortactin, and Lifeact-RFP with N-WASP-GFP on individual nanopillars with 15-s time interval show correlated dynamic fluctuations. (*G*) The quantified Pearson correlation coefficient between the dynamics of Lifeact-RFP and 5 F-actin related proteins, $n = 89$ to 220 trajectories for each protein (see *SI Appendix*, Table S3 for detailed statistics). Welch's *t* test, *P* values indicated in *C*, *D*, and *G*, ****$P < 0.0001$; ns = 0.08. Error bars represent SEM. (Scale bar, 10 μm [*A*, full image], 2 μm [*A*, kymograph, horizontal), 2 min (*A*, kymograph, vertical].)

(33) to modulate actin cytoskeleton (34, 35) (Fig. 4*A*). A previous in vitro study indicates that they are able to induce curvature-dependent F-actin assembly on vesicle membranes (36). Therefore, we hypothesized that these proteins recognize the topography-induced membrane curvatures to induce F-actin accumulation on nanostructures.

Three Toca family proteins GFP-FBP17, Toca1-GFP, or CIP4-GFP were all shown to accumulate at the ends of nanobars similar to Arp2/3 complex, Cortactin, and N-WASP (Fig. 4*B* and *SI Appendix*, Fig. S3 *A* and *B*). The accumulation is often more pronounced under the nucleus due to the lower fluorescence background inside the nucleus, and high protein expression induces tubule formation (37). For the following studies, we focus on widely expressed FBP17 that also shows the strongest response among the 3 members. We further confirmed the curvature response of FBP17 using wedged nanobars which are narrow (high curvature) at one end and wide (low curvature) at the other end (Fig. 4*C*). GFP-FBP17 has a much higher fluorescence intensity at the narrow end than the wide end on the same nanobar (Fig. 4 *D* and *E*).

Taking advantage of the gradient geometry generation by EBL fabrication, we quantitatively probed the range of curvature values that can induce FBP17 accumulation using gradient nanobar arrays with the bar width varying from 100 nm to 1,000 nm (Fig. 4*F*). The width of each nanobar determines the curvature value at its ends. To corroborate the transient transfection studies used in Fig. 4 *B* and *D*, we used anti-FBP17 immunostaining to probe the spatial distribution of endogenous FBP17. The averaged nanobar images of different widths show that endogenous FBP17 accumulates strongly to the 2 ends of nanobars with a width smaller than 400 nm, but do not show an obvious response to a width of 500 nm or above (Fig. 4*G*). The curvature threshold for FBP17 accumulation is similar to that for F-actin. The trend is more clearly shown in the quantitative analysis in Fig. 4*H*.

The role of FBP17 is validated by constructing a truncated FBP mutant (FBP17ΔSH3), which contains the curvature-sensing F-BAR domain but not the C-terminal SH3 domain for inducing actin polymerization (Fig. 5*A*). Spatial distribution of both GFP-FBP17 and mCherry-FBP17ΔSH3 show preferential accumulation on the ends of nanobars (Fig. 5*B*), indicating that FBP17ΔSH3 maintains the ability to recognize nanostructure-induced plasma membrane curvature (Fig. 5*C*).

Interestingly, overexpression of mCherry-FBP17ΔSH3 abolishes the nanostructure-induced F-actin accumulation on nanopillars and nanobar ends. As shown in Fig. 5*D*, U2OS cells cotransfected with GFP-FBP17 and Lifeat-RFP show clear accumulation of both

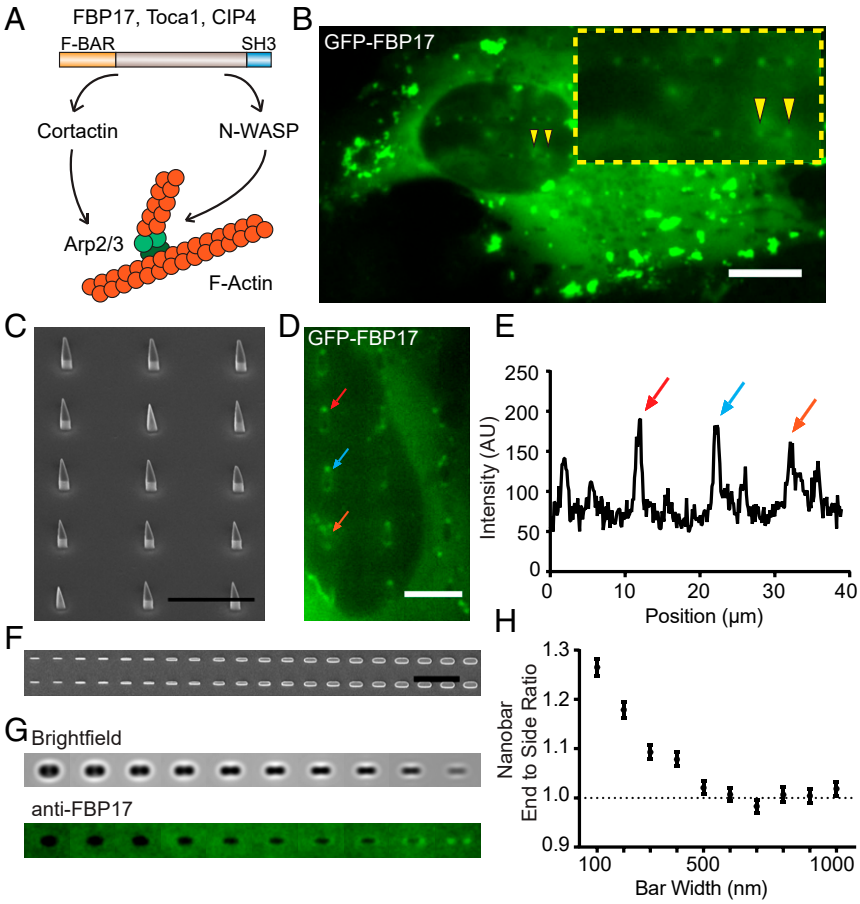

Fig. 4. FBP17 preferentially accumulates at high curvature locations induced by nanostructures. (*A*) A schematic drawing of Toca family proteins activating Arp2/3-mediated actin polymerization. (*B*) GFP-FBP17 preferentially accumulates to the ends of nanobars. (*C*) An SEM image of wedged nanobars. (*D*) On wedged nanobars, GFP-FBP17 shows a much higher signal at the narrow end (high curvature) than the wide end (low curvature). (*E*) An intensity plot along a line of wedged nanobars illustrates that GFP-FBP17 prefers the narrow ends of wedged nanobars. (*F*) A gradient nanobar array with 2-μm length, 800-nm height, 5-μm center-to-center distance between nanobars, and a variable width from 100 to 1,000 nm with 100-nm increment. Each width is represented by 2 bar columns in the array. (*G*) The averaged nanobar images of anti-FBP17 immunostaining for 10 different nanobar widths, from the largest 1,000 nm to the smallest 100 nm. n = 1,278 to 1,728 nanobars (see *SI Appendix*, Table S4 for detailed statistics). (*H*) The measured nanobar end-to-side ratio of anti-FBP17 decreases with the bar width but levels off when the bar width is 500 nm or larger. Error bars represent SEM.

GFP-FBP17 and Lifeact-RFP at the ends of nanobars. On the other hand, in cells transfected with mCherry-FBP17ΔSH3, the preferential accumulation of Lifeact-GFP at the same locations are largely eliminated (Fig. 5*E*). Quantitative analysis shows that the nanobar end-to-side ratio of Lifeact in mCherry-FBP17ΔSH3 transfected cells is significantly lower than that of GFP-FBP17 transfected cells (Fig. 5*F*). The decrease of F-actin intensity on nanopillars positively correlates with the expression level of FBP17ΔSH3 (*SI Appendix*, Fig. S3 *C* and *D*). Similarly, the reduction of Arp2/3 at nanobar ends was also observed in cells overexpressing mCherry-FBP17ΔSH3 (Fig. 5 *G* and *H* and the corresponding full images in *SI Appendix*, Fig. S4). These results indicate that the accumulation of FBP17ΔSH3 on membrane curvatures interferes with nanostructure-induced activation of Arp2/3 complex and prevents F-actin polymerization.

Nanostructure-Induced F-Actin Polymerization Reduces the Formation of Actin Stress Fibers and Mature Focal Adhesions. Actin polymerization is involved in many cellular processes. Our previous study shows that nanostructure-induced membrane curvature enhances clathrin-mediated endocytosis (28), so we examine whether F-actin assembly at nanostructures is related to the endocytosis process. Inhibiting clathrin-mediated endocytosis by Pitstop 2 does not significantly affect F-actin accumulation or its dynamic fluctuations on nanopillars (*SI Appendix*, Fig. S5 *A–C*) Similarly, the spatially biased accumulation toward the ends of nanobars persists after Pitstop 2 treatment (*SI Appendix*, Fig. S5 *D* and *F*). When the nanostructure-induced F-actin accumulation is blocked by overexpression of mCherry-FBP17ΔSH3, the preference of the clathrin-adaptor protein AP2-GFP toward the ends of nanobars is reduced but does not fully disappear (*SI Appendix*, Fig. S5 *E* and *G*). This result suggests that nanostructure-induced F-actin is not exclusively involved in the endocytosis process.

In addition to endocytosis, we also probed how nanostructure-induced formation of branched F-actin affects the formation of linear F-actin stress fibers and their associated focal adhesion complexes, which are essential for mechanotransduction, cell adhesion, contraction, and migration. For this purpose, we examined the cellular distribution of F-actin and 3 core protein components of mature focal adhesions, vinculin, paxillin, and Myosin II. The results show that, unlike F-actin that preferentially accumulates at the ends of nanobars, vinculin, paxillin, and Myosin IIb show very little signal either at the ends or along the sidewalls of nanobars (Fig. 6 *A* and *B*). Occasionally, vinculin and paxillin show weak fluorescence signal on nanobars, but there is no preference to the ends. Therefore, nanostructure-induced F-actin fibers do not appear to participate in mature focal adhesions.

When stained by phalloidin and anti-paxillin, cells cultured on flat areas show a network of long and straight stress fibers whose ends colocalize with large paxillin patches of similarly oriented and elongated focal adhesions (Fig. 6*C*). On the other hand, cells cultured on nanopillar areas show very different F-actin patterns with clear accumulation around nanopillars, illustrating the regularly

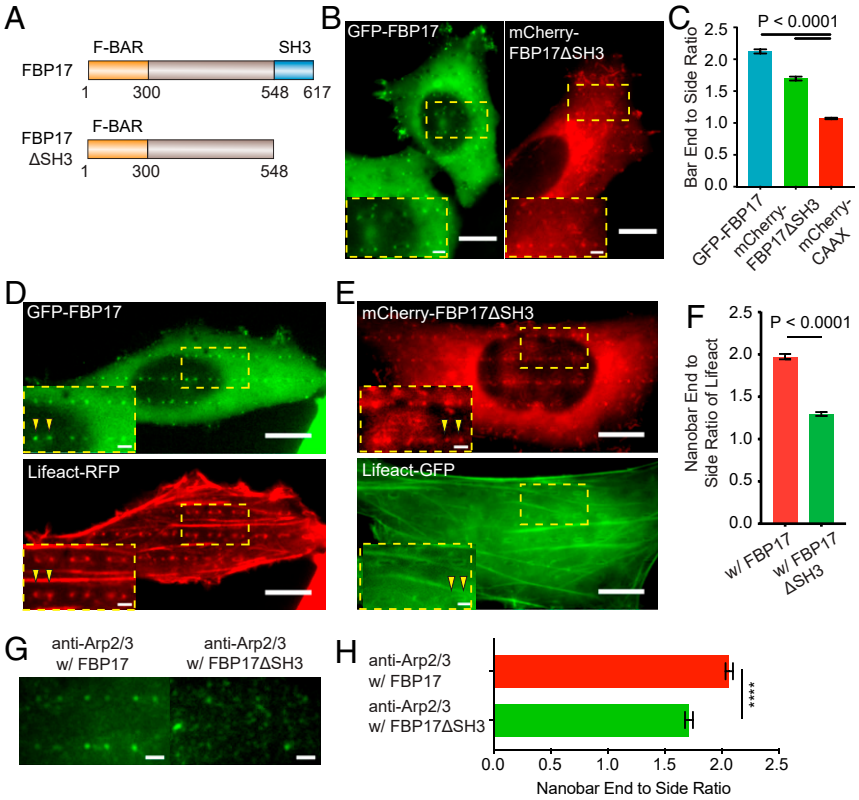

Fig. 5. FBP17ΔSH3 reduces the curvature-dependent F-actin accumulation at nanostructures. (*A*) Illustrations of the full-length FBP17 and the truncated FBP17ΔSH3 plasmid constructs. (*B*) Both GFP-FBP17 (*Left*) and mCherry-FBP17ΔSH3 (*Right*) preferentially accumulate at the ends of nanobars. (*C*) Quantified nanobar end-to-side ratios of GFP-FBP17 and mCherry-FBP17ΔSH3 and mCherry-CAAX. (*D*) A U2OS cell cotransfected with GFP-FBP17 and Lifeact-RFP shows that both FBP17 and F-actin accumulate to the ends of nanobars. (*E*) A U2OS cell cotransfected with mCherry-FBP17ΔSH3 and Lifeact-GFP shows that the accumulation of FBP17ΔSH3 persists but the accumulation of F-actin at ends of nanobars is mostly eliminated. (*F*) Quantified nanobar end-to-side ratios of Lifeact in U2OS cells coexpressing GFP-FBP17 or mCherry-FBP17ΔSH3. (*G* and *H*) Overexpression of mCherry-FBP17ΔSH3 reduces the preference of endogenous Arp2/3 to the nanobar ends. Welch's *t* test with *P* values indicated in *C* and *F*, ****$P < 0.0001$. Error bars represent SEM. (Scale bars, 10 μm [*B*, *D*, and *E*: full image], 2 μm [*B*, *D*, and *E*: zoom-in, *G*].)

spaced arrays but much fewer stress fibers. Paxillin staining also shows a highly diffusive signal in cell and the paxillin patches are much smaller in size. Statistical analysis shows that the ratio of stress fiber area to cell area is reduced by 45% on nanopillars (Fig. 6*E*) and the number of large focal adhesion (>0.5 μm^2) per cell decreased by 90% (Fig. 6*F*). When treated with blebbistatin, a specific Myosin II inhibitor that is known to cause disassembly of actin stress fibers (38), the long F-actin stress fibers and the large paxillin patches on the flat surface have mostly disappeared (Fig. 6*D*). Interestingly, blebbistatin treatment did not block nanostructure-induced F-actin formation on nanopillars (Fig. 6*D*). Furthermore, quantitative analysis shows that the total intensity of F-actin on nanopillars per cell has almost doubled after blebbistatin treatment (Fig. 6*G*). Quantitative analysis shows that nanostructure-induced F-actin formation and stress fiber F-actin negatively correlated with each other to induce whole-cell F-actin reorganization on nanopillars (*SI Appendix*, Fig. S6). This anticorrelation could be due to their competition for the same pool of actin monomer or due to other nanostructure-induced changes of mechanotransduction (39). These results also agree with the previous report that impairment of stress fibers prohibits the stabilization of nascent focal adhesions and therefore the formation of mature focal adhesions (40).

Conclusions

In this work, we show that local membrane curvature induced by surface topography serves as a biochemical signal to induce actin reorganization inside cells (Fig. 7). Curvature-sensing proteins, FBP17 in particular, are able to recognize topography-induced curvature of a limited range (diameter of the curvature <400 nm) to activate downstream signaling components including N-WASP, Cortactin, and the Arp2/3 complex to nucleate the formation of branched F-actin. This topography-induced F-actin actively impacts multiple cellular processes, such as endocytosis, stress fiber organization, and focal adhesion maturation. While this work does not preclude other potential mechanisms, it supports the

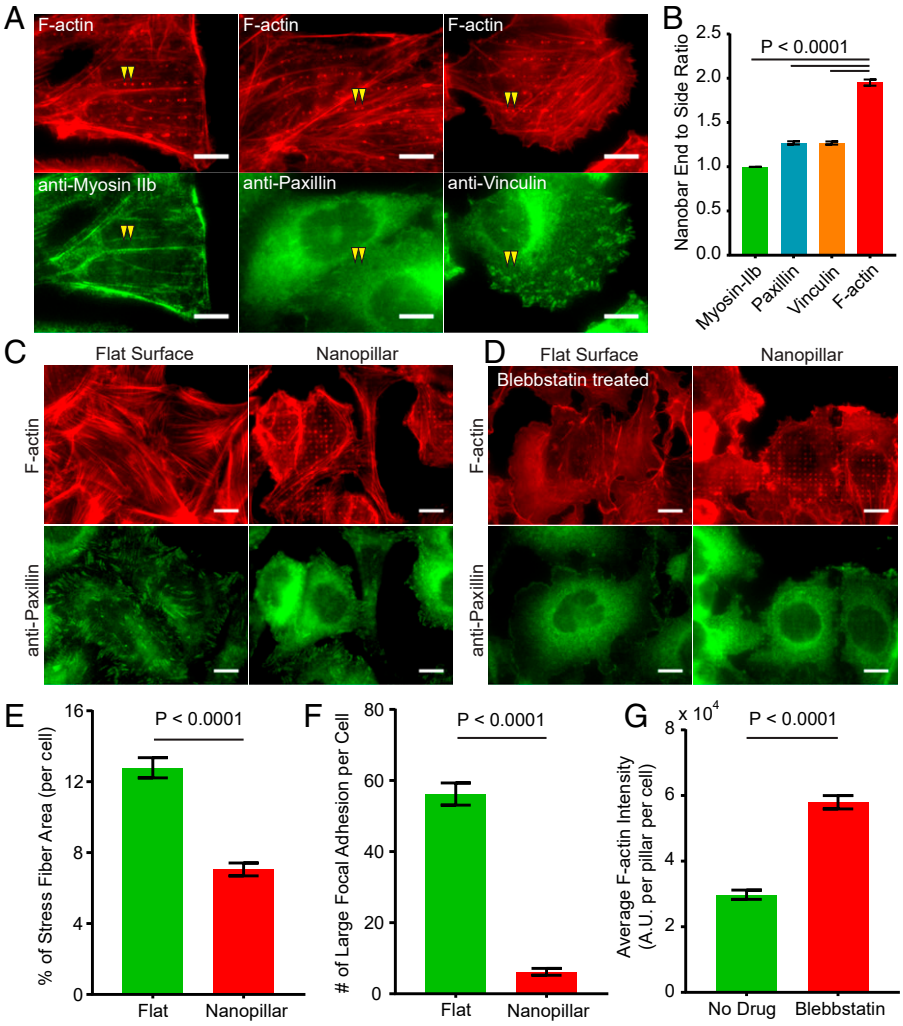

Fig. 6. Nanostructure-induced F-actin accumulation reduces the formation of stress fibers and mature focal adhesions. (*A*) Nanostructure-induced F-actin formed at the ends of nanobars does not colocalize with Myosin IIb, paxillin, or vinculin, core protein components of mature focal adhesion. (*B*) Quantified nanobar end-to-side ratios for F-actin, Myosin-IIb, paxilin, and vinculin. (*C*) Anti-paxillin staining and phalloidin staining of F-actin show a clear reduction of F-actin stress fibers and the size of focal adhesion patches on nanopillars as compared with flat areas. (*D*) Blebbistatin treatment (25 μM, 30 min) has largely removed the F-actin stress fibers and paxillin patches in U2OS cells on both flat areas and nanopillars. On the other hand, the F-actin accumulation on nanopillars still persists. (*E*) The percentage of stress fiber area for U2OS cells cultured on flat surfaces is much larger than that on nanopillar arrays. (*F*) The number of large paxillin focal adhesion patches (>0.5 μm^2) per cell is significantly reduced on nanopillar arrays as compared with that on flat areas. (*G*) The F-actin intensity per nanopillar per cell increased dramatically upon blebbistatin treatment. Welch's *t* test with *P* values are indicated. Error bars represent SEM. (Scale bars, 10 μm [*A*, *C*, and *D*].)

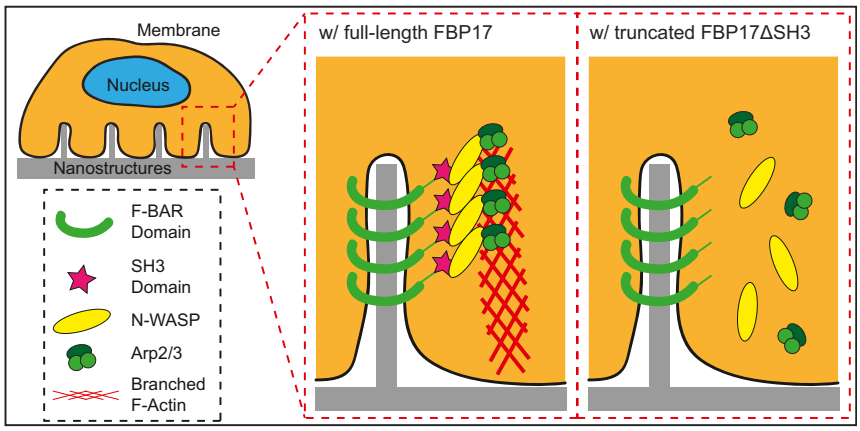

Fig. 7. Schematic illustration of curvature-dependent F-actin formation around nanopillars. The F-BAR domain of FBP17 recognizes nanopillar-induced membrane curvature, while the SH3 domain of FBP17 interacts with N-WASP to promote Arp2/3-initiated F-actin polymerization. Truncated FBP17ΔSH3 recognizes nanopillar-induced membrane curvature but is not able to promote F-actin polymerization.

hypothesis that topography-induced membrane curvature is a key mechanism underlying how cells recognize and respond to surface topography. The knowledge gained here will assist the effort to design material surface topography to achieve desired cell behavior.

Materials and Methods

Nanostructure Fabrication. The SiO_2 nanostructures in this work were fabricated on quartz coverslips by electron-beam lithography and reactive ion etching (28, 41). The patterns of nanostructures were written by electron-beam lithography (Raith 150) and developed in xylene. Metal masks were formed by sputtering with 100 nm of Cr and liftoff in acetone. The quartz nanostructures were generated by anisotropic reactive ion etching with CHF_3 and O_2 mixture (AMT 8100 etcher, Applied Materials).

Cell Culture, Transfection, and Live Cell Imaging. U2OS cells were used in this study. Before cell plating, nanostructure substrates were sterilized by O_2 plasma and coated in 0.1% gelatin. U2OS cells were cultured for at least 18 h before fixation or imaging. Electroporation was used for plasmid transfection. Live-cell imaging was carried out using an epifluorescence microscope (Leica DMI 6000B). During the imaging, cells were maintained at 37 °C with 5% CO_2 in an onstage incubator (INUBSF-ZILCS, Tokai Hit).

Immunostaining and Imaging. Cells were fixed in 4% paraformaldehyde, washed by PBS, permeabilized in 0.1% Triton X-100, blocked in 1% BSA, and followed by staining with 2 μg/mL secondary antibodies. The prepared samples were imaged by epifluorescence microscope (Leica DMI 6000B) or confocal microscopy (Olympus FV1000)

Quantitative Analysis. For the quantitative analysis, the images were processed by a rolling ball algorithm with a radius of 12 pixels. The circle masks were created to cover the pillar area. The pixel intensities within the masks were integrated and the intensity with the same nanopillar diameter was averaged. The ratios of F-actin were calculated by dividing the mean intensities of F-actin with GFP-CAAX.

Statistics. Sample sizes were validated using power analysis similar to previous work (28). Welch's *t* tests (unpaired, 2 tailed, not assuming equal SD) and the Kolmogorov–Smirnov test (unpaired, not assuming Gaussian distribution) were used to evaluate the significance. All tests were performed using Prism (GraphPad Software). Data are presented as mean ± SEM or mean ± SD as stated in the figure captions.

ACKNOWLEDGMENTS. We thank C. Kaplan in D.G.D. group, Q. Ong in B.C. group, and E. C. Norby in J. Theriot group for helpful advice. Nanofabrication and characterization were performed in Stanford Nano Shared Facilities (SNSF) and Stanford Nanofabrication Facility (SNF). This work was funded by NIH (R01GM117263 to B.C. and R35GM1181149 to D.G.D.), the Packard Foundation (to B.C.), Heart Rhythm Society (to F.S.), and Arnold and Mabel Beckman Foundation (to M.A.).

1. M. J. Dalby, N. Gadegaard, R. O. C. Oreffo, Harnessing nanotopography and integrin-matrix interactions to influence stem cell fate. *Nat. Mater.* **13**, 558–569 (2014).
2. P. Viswanathan *et al.*, 3D surface topology guides stem cell adhesion and differentiation. *Biomaterials* **52**, 140–147 (2015).
3. W. Chen, Y. Shao, X. Li, G. Zhao, J. Fu, Nanotopographical surfaces for stem cell fate control: Engineering mechanobiology from the bottom. *Nano Today* **9**, 759–784 (2014).
4. D.-H. Kim, P. P. Provenzano, C. L. Smith, A. Levchenko, Matrix nanotopography as a regulator of cell function. *J. Cell Biol.* **197**, 351–360 (2012).
5. Y.-N. Wu *et al.*, Substrate topography determines the fate of chondrogenesis from human mesenchymal stem cells resulting in specific cartilage phenotype formation. *Nanomedicine* **10**, 1507–1516 (2014).
6. B. K. K. Teo *et al.*, Nanotopography modulates mechanotransduction of stem cells and induces differentiation through focal adhesion kinase. *ACS Nano* **7**, 4785–4798 (2013).
7. K. Yang *et al.*, Nanotopographical manipulation of focal adhesion formation for enhanced differentiation of human neural stem cells. *ACS Appl. Mater. Interfaces* **5**, 10529–10540 (2013).
8. S. Musah *et al.*, Substratum-induced differentiation of human pluripotent stem cells reveals the coactivator YAP is a potent regulator of neuronal specification. *Proc. Natl. Acad. Sci. U.S.A.* **111**, 13805–13810 (2014).
9. T. U. Luu, S. C. Gott, B. W. K. Woo, M. P. Rao, W. F. Liu, Micro- and nanopatterned topographical cues for regulating macrophage cell shape and phenotype. *ACS Appl. Mater. Interfaces* **7**, 28665–28672 (2015).
10. C.-Y. Yang, L.-Y. Huang, T.-L. Shen, J. A. Yeh, Cell adhesion, morphology and biochemistry on nano-topographic oxidized silicon surfaces. *Eur. Cell. Mater.* **20**, 415–430 (2010).
11. J. Lee *et al.*, The control of cell adhesion and viability by zinc oxide nanorods. *Biomaterials* **29**, 3743–3749 (2008).
12. P. Formentín *et al.*, Effects of SiO_2 micropillar arrays on endothelial cells' morphology. *N. Biotechnol.* **33**, 781–789 (2016).
13. S. Bonde *et al.*, Tuning InAs nanowire density for HEK293 cell viability, adhesion, and morphology: Perspectives for nanowire-based biosensors. *ACS Appl. Mater. Interfaces* **5**, 10510–10519 (2013).
14. M. Jasnin, M. Ecke, W. Baumeister, G. Gerisch, Actin organization in cells responding to a perforated surface, revealed by live imaging and cryo-electron tomography. *Structure* **24**, 1031–1043 (2016).
15. H. Persson *et al.*, Vertical oxide nanotubes connected by subsurface microchannels. *Nano Res.* **5**, 190–198 (2012).
16. K. S. Beckwith, S. P. Cooil, J. W. Wells, P. Sikorski, Tunable high aspect ratio polymer nanostructures for cell interfaces. *Nanoscale* **7**, 8438–8450 (2015).
17. A. L. Rosa, M. M. Beloti, Rat bone marrow cell response to titanium and titanium alloy with different surface roughness. *Clin. Oral Implants Res.* **14**, 43–48 (2003).
18. T. S. N. Silva, D. C. Machado, C. Viezzer, A. N. Silva Júnior, M. G. Oliveira, Effect of titanium surface roughness on human bone marrow cell proliferation and differentiation: An experimental study. *Acta Cir. Bras.* **24**, 200–205 (2009).
19. E. Eisenbarth, D. Velten, M. Müller, R. Thull, J. Breme, Nanostructured niobium oxide coatings influence osteoblast adhesion. *J. Biomed. Mater. Res. A* **79**, 166–175 (2006).
20. M. J. Dalby *et al.*, The control of human mesenchymal cell differentiation using nanoscale symmetry and disorder. *Nat. Mater.* **6**, 997–1003 (2007).
21. W. Chen *et al.*, Nanotopography influences adhesion, spreading, and self-renewal of human embryonic stem cells. *ACS Nano* **6**, 4094–4103 (2012).
22. L. C. Y. Lee *et al.*, Nanotopography controls cell cycle changes involved with skeletal stem cell self-renewal and multipotency. *Biomaterials* **116**, 10–20 (2017).

23. J. Rychly, B. Nebe, Interface biology of implants. *Cell Adhes. Migr.* **3**, 390–394 (2009).
24. F. F. B. Hulshof *et al*., NanoTopoChip: High-throughput nanotopographical cell instruction. *Acta Biomater.* **62**, 188–198 (2017).
25. F. Santoro *et al*., Revealing the cell-material interface with nanometer resolution by focused ion beam/scanning electron microscopy. *ACS Nano* **11**, 8320–8328 (2017).
26. L. Hanson, Z. C. Lin, C. Xie, Y. Cui, B. Cui, Characterization of the cell-nanopillar interface by transmission electron microscopy. *Nano Lett.* **12**, 5815–5820 (2012).
27. T. Berthing *et al*., Cell membrane conformation at vertical nanowire array interface revealed by fluorescence imaging. *Nanotechnology* **23**, 415102 (2012).
28. W. Zhao *et al*., Nanoscale manipulation of membrane curvature for probing endocytosis in live cells. *Nat. Nanotechnol.* **12**, 750–756 (2017).
29. X. Li *et al*., A nanostructure platform for live-cell manipulation of membrane curvature. *Nat. Protoc.* **14**, 1772–1802 (2019).
30. M. A. Chesarone, B. L. Goode, Actin nucleation and elongation factors: Mechanisms and interplay. *Curr. Opin. Cell Biol.* **21**, 28–37 (2009).
31. J. D. Rotty, C. Wu, J. E. Bear, New insights into the regulation and cellular functions of the ARP2/3 complex. *Nat. Rev. Mol. Cell Biol.* **14**, 7–12 (2013).
32. C. Mim, V. M. Unger, Membrane curvature and its generation by BAR proteins. *Trends Biochem. Sci.* **37**, 526–533 (2012).
33. H.-Y. H. Ho *et al*., Toca-1 mediates Cdc42-dependent actin nucleation by activating the N-WASP-WIP complex. *Cell* **118**, 203–216 (2004).
34. P. J. Carman, R. Dominguez, BAR domain proteins-a linkage between cellular membranes, signaling pathways, and the actin cytoskeleton. *Biophys. Rev.* **10**, 1587–1604 (2018).
35. K. Tsujita *et al*., Coordination between the actin cytoskeleton and membrane deformation by a novel membrane tubulation domain of PCH proteins is involved in endocytosis. *J. Cell Biol.* **172**, 269–279 (2006).
36. K. Takano, K. Toyooka, S. Suetsugu, EFC/F-BAR proteins and the N-WASP-WIP complex induce membrane curvature-dependent actin polymerization. *EMBO J.* **27**, 2817–2828 (2008).
37. A. Frost *et al*., Structural basis of membrane invagination by F-BAR domains. *Cell* **132**, 807–817 (2008).
38. A. M. Pasapera, I. C. Schneider, E. Rericha, D. D. Schlaepfer, C. M. Waterman, Myosin II activity regulates vinculin recruitment to focal adhesions through FAK-mediated paxillin phosphorylation. *J. Cell Biol.* **188**, 877–890 (2010).
39. C. S. Hansel *et al*., Nanoneedle-mediated stimulation of cell mechanotransduction machinery. *ACS Nano* **13**, 2913–2926 (2019).
40. P. W. Oakes, Y. Beckham, J. Stricker, M. L. Gardel, Tension is required but not sufficient for focal adhesion maturation without a stress fiber template. *J. Cell Biol.* **196**, 363–374 (2012).
41. L. Hanson *et al*., Vertical nanopillars for in situ probing of nuclear mechanics in adherent cells. *Nat. Nanotechnol.* **10**, 554–562 (2015).